Hydrogen Storage in New Metal−Organic Frameworks

David J. Tranchemontagne,[†] Kyo Sung Park,[†] Hiroyasu Furukawa,*[,†,⊥] Juergen Eckert,[§] Carolyn B. Knobler,[†] and Omar M. Yaghi[†,‡,⊥]

[†]Center for Reticular Chemistry, UCLA−DOE Institute for Genomics and Proteomics, and Department of Chemistry and Biochemistry, University of California−Los Angeles, 607 East Charles E. Young Drive, Los Angeles, California 90095, United States
[‡]NanoCentury KI and Graduate School of EEWS (WCU) KAIST, Daejeon 305-701, Korea
[§]Department of Chemistry, 4202 East Fowler Avenue, University of South Florida, Tampa, Florida 33620, United States

S Supporting Information

ABSTRACT: Five new metal−organic frameworks (MOFs, termed MOF-324, 325, 326 and IRMOF-61 and 62) of either short linkers (pyrazolecarboxylate and pyrazaboledicarboxylate) or long and thin alkyne functionalities (ethynyldibenzoate and butadiynedibenzoate) were prepared to examine their impact on hydrogen storage in MOFs. These compounds were characterized by single-crystal X-ray diffraction, and their low-pressure and high-pressure hydrogen uptake properties were investigated. In particular, volumetric excess H_2 uptake by MOF-324 and IRMOF-62 outperforms MOF-177 up to 30 bar. Inelastic neutron-scattering studies for MOF-324 also revealed strong interactions between the organic links and hydrogen, in contrast to MOF-5 where the interactions between the Zn_4O unit and hydrogen are the strongest. These data also show that smaller pores and polarized linkers in MOFs are indeed advantageous for hydrogen storage.
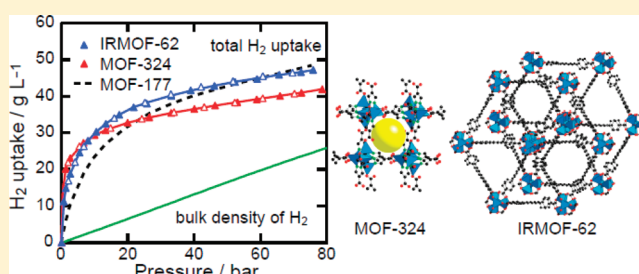
INTRODUCTION

To date, as a result of environmental concerns over fossil fuel consumption, increasing attention has been given to utilization of cleaner energy sources, such as methane and hydrogen.[1] The storage of hydrogen in porous materials is advantageous since it can be compacted within the pores.[2] Metal−organic frameworks (MOFs)[3] offer many opportunities for testing the effect of pore size and functionality on the hydrogen storage capacity. We can take advantage of the versatile nature of MOF chemistry by changing the combination of organic links and metal sources, allowing various pore dimensions and functionalities to be obtained. Pore size distributions in many MOFs are greater than 10 Å, owing in part to the large dimensions of the secondary building unit (SBU); the distance between two carboxylate carbons in the SBUs (e.g., 8.5 Å for $Zn_4O(CO_2)_6$,[3a] 6.7 Å for $Cu_2(CO_2)_4$)[4] is close to the definition of ultramicropore (<7 Å).[5] On the other hand, some MOFs have smaller pore diameters, leading to moderately stronger adsorbent−adsorbate interactions. Despite this, such materials usually have either slow gas diffusion rates or low surface areas. The size and functionalizations of the micropores must both be optimized to best utilize the walls of the adsorbents without losing the intrinsic porosity of the MOFs.

In this study, we focused on making MOFs with small pores from either short organic links or from long thin links which would allow interpenetration that leads to small pores, as depicted in Scheme 1. Using the organic links 4-pyrazolecarboxylic acid (H_2PyC), 2,8-pyrazaboledicarboxylic acid (H_2PzDC), 4,4,8,8-tetraethyl-2,8-pyrazaboledicarboxylic acid

Scheme 1. Short Dicarboxylic Acids Used in MOF Synthesis: (a) Oxalic Acid, (b) Acetylene Dicarboxylic Acid, (c) Terephthalic Acid, and (d) 4-Pyrazolecarboxylic Acid (H_2PyC)
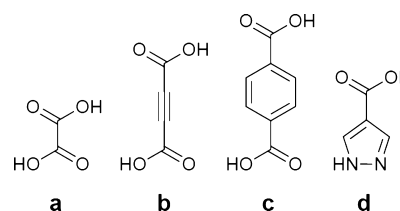
(H_2Et-PzDC), ethynyldibenzoic acid (H_2EDB), and butadiynedibenzoic acid (H_2BDB), we synthesized five new MOFs: $Zn_3(OH)[(PyC)_2(HPyC)]$ (MOF-324) and $Cu_3[(Cu_3O)(PyC)_3(NO_3)]_2$ (MOF-325), based on in situ formation of a short organic link to provide small pores, $Zn_4O(Et$-PzDC$)_3$ (MOF-326), which utilizes the polarizable pyrazabole unit, $Zn_4O(EDB)_3$ (IRMOF-61), and $Zn_4O(BDB)_3$ (IRMOF-62), which impart interpenetration through alkyne-containing links to affect the pore size. The structures of these MOFs produced by solvothermal reactions were determined by single-crystal X-ray diffraction analyses. In particular, both MOF-324 and IRMOF-62 have small pores and high surface areas and excellent cryogenic H_2 (77 K) uptakes at 1 bar. Based on the
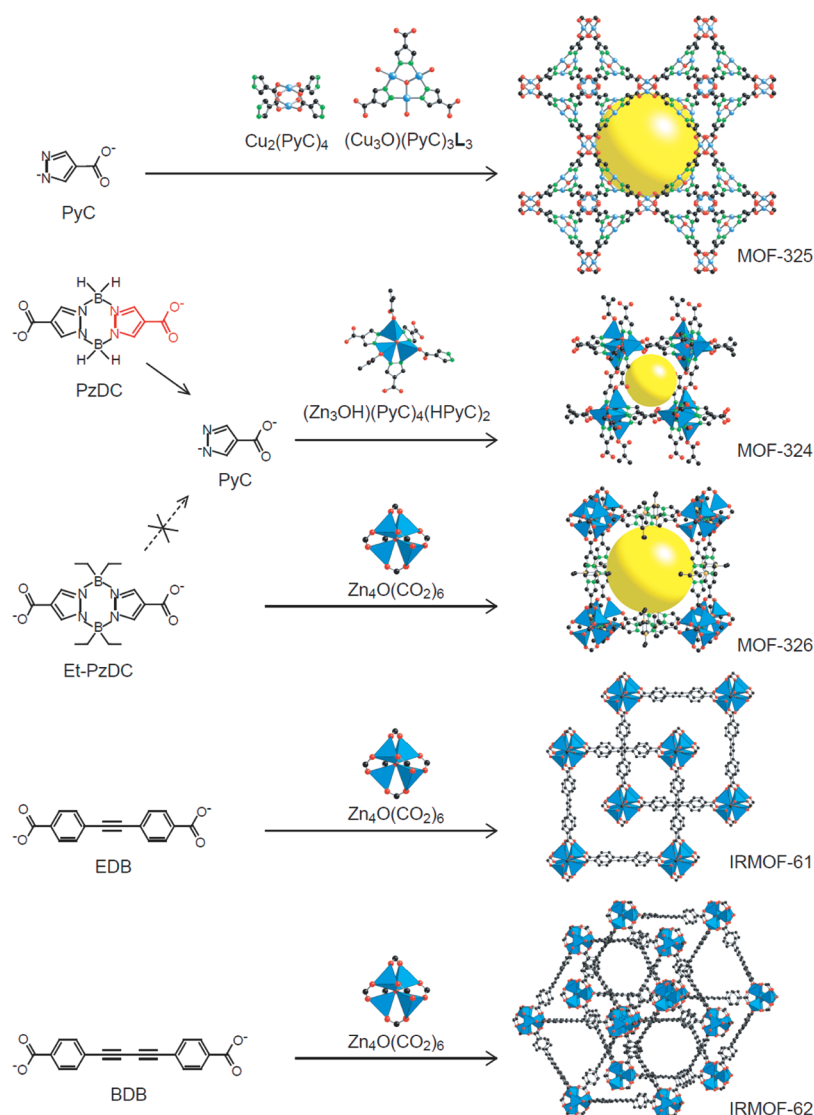
Figure 1. Molecular structures of organic links and their abbreviations (left). These links are connected with SBUs (middle) to form MOFs, whose X-ray single-crystal structures are shown at the right. The yellow sphere represents the largest sphere that would occupy the cavity without contacting the interior van der Waals surface. Zn, blue polyhedron; Cu, blue; O, red; C, black; B, orange; N, green; all hydrogen atoms are omitted for clarity.

inelastic neutron-scattering (INS) experiments, we reveal that MOF-324 demonstrates strong interactions between hydrogen and the host material in comparison to MOF-5, which also supported the data from the isosteric heats of H_2 adsorption (Q_{st}).[6a]

■ EXPERIMENTAL SECTION

Organic Links. 4-Pyrazolecarboxylic acid (H_2PyC) was purchased from Aldrich. 2,8-Pyrazaboledicarboxylic acid (H_2PzDC) and 4,4,8,8-tetraethyl-2,8-pyrazaboledicarboxylic acid (H_2Et-PzDC) were synthesized according to literature methods.[7] Synthetic procedures and characterization of H_2EDB and H_2BDB are described in the Supporting Information. The molecular structures of these links are depicted in Figure 1.

Synthesis and Characterization of MOFs and IRMOFs. For easy reference, the formulas for three MOFs and two IRMOFs and their crystal unit cell parameters are listed in Table 1. Zinc nitrate tetrahydrate was purchased from EM science. Copper nitrate hemipentahydrate, zinc acetate dihydrate, N,N-dimethylformamide (DMF), 1-methyl-2-pyrro-

lidinone (NMP), and triethylamine were purchased from Fisher Scientific. N,N-Diethylformamide (DEF) was obtained from BASF. All purchased materials were used without further purification. Thermogravimetric analyses (TGA) were performed on a TA Q500 thermal analysis system with the sample held in a platinum pan in a continuous nitrogen flow atmosphere. Fourier transform infrared (FT-IR) spectra were obtained by using a Nicolet FT-IR Impact 400 system and KBr pellet samples. The elemental analysis (EA) was performed using a Thermo Flash EA1112 combustion CHNS analyzer.

Powder and Single-Crystal X-ray Diffraction Analyses. Powder X-ray diffraction (PXRD) patterns were collected with a Bruker AXS D8 Advanced diffractometer operated at 40 kV and 40 mA with monochromated Cu $K\alpha$ radiation ($\lambda = 1.540\ 6$ Å) and with a scan speed of 1 s/step and a step size of 0.05°. The simulated PXRD patterns were calculated from single-crystal data using the PowderCell 2.3 software suite.[8]

Single-crystal X-ray diffraction (SXRD) data were collected on a Bruker SMART Apex diffractometer equipped with a CCD area detector and operated at 1800 W power (45 kV, 40

13144

dx.doi.org/10.1021/jp302356q | J. Phys. Chem. C 2012, 116, 13143−13151

Table 1. Crystal Structure Data for Synthesized MOFs

MOF	organic link	chemical formula[a] space group; a, b, c (Å) α, β, γ (deg); V (Å^3); Z
MOF-324	PyC	$Zn_3(OH)[(PyC)_2(HPyC)]\cdot(DMF)(H_2O)_5$
		$Pa\overline{3}$; 20.123, 20.123, 20.123
		90, 90, 90; 8148.5; 8
MOF-325	PyC	$Cu_3[(Cu_3O)$
		$(PyC)_3(NO_3)]_2\cdot(DEF)_{18}(NMP)_3(H_2O)_8$
		$Fm\overline{3}m$; 42.606, 42.606, 42.606
		90, 90, 90; 77342; 16
MOF-326	Et-PzDC	$Zn_4O(Et\text{-}PzDC)_3\cdot(DMF)_{16}(H_2O)_3$
		$Fm\overline{3}m$; 33.410, 33.410, 33.410
		90, 90, 90; 37294; 8
IRMOF-61	EDB	$Zn_4O(EDB)_3\cdot(DMF)_{17}(H_2O)_7$
		$P4_2/ncm$; 19.7213, 19.7213, 39.411
		90, 90, 90; 15328.0; 4
IRMOF-62	BDB	$Zn_4O(BDB)_3\cdot(DMF)_{10}(H_2O)_3$
		$P3_212$; 31.114, 31.114, 39.280
		90, 90, 120; 32931; 12

[a]DMF = *N,N*-dimethylformamide; DEF = *N,N*-diethylformamide; NMP = 1-methyl-2-pyrrolidinone.

mA) to generate (graphite-monochromated) Mo Kα radiation (λ = 0.710 73 Å). The data were collected with phi and omega scans. The frames were integrated using the Bruker SAINT Software package (Ver. 6.01). The reflection data were corrected for absorption by using Bruker SADABS and solved with the Bruker SHELXTL (Ver. 6.14) Software package using direct methods.

Adsorption Measurements. Low-pressure N_2, Ar, and H_2 adsorption measurements (up to 760 torr) were performed on an Autosorb-1 (Quantachrome) volumetric analyzer.[6b,c] Liquid nitrogen and argon baths were used for N_2 and H_2 (77 K) and Ar and H_2 (87 K). Gravimetric high-pressure H_2 adsorption isotherms were measured by use of GHP-300 from the VTI Corporation.[6b,c] A Rubotherm magnetic suspension balance MC-5 was used to measure the change in mass of samples suspended within a tube under a chosen atmosphere. When H_2 gas was used, condensable impurities were removed with a liquid nitrogen trap. The adsorbate was added incrementally, and data points were recorded when no further change in mass was observed. To obtain the excess adsorption isotherm, all data points were corrected for buoyancy and for the thermal gradient that arises between the balance (313 K) and the sample bucket.[6b,c] Ultrahigh-purity grade N_2, Ar, H_2, and He (99.999% purity) gases were used throughout the adsorption experiments.

Inelastic Neutron Scattering. Inelastic neutron-scattering (INS) spectra were collected at a temperature of 10 K on the quasielastic neutron spectrometer at the Intense Pulsed Neutron Source (IPNS) at Argonne National Laboratory. Successive loading of material with hydrogen was carried out in situ at 77 K after first obtaining a spectrum of the "blank" sample. The spectra shown in Figure 6 were obtained by subtracting the blank spectrum.

$Zn_3(OH)[(PyC)_2(HPyC)]\cdot(DMF)(H_2O)_5$, MOF-324. A solid mixture of $Zn(NO_3)_2\cdot4H_2O$ (190 mg, 0.72 mmol) and H_2PzDC (63 mg, 0.25 mmol) was dissolved in 11.5 mL of DMF and 6.5 mL of H_2O (2:1 v/v) in a 20 mL vial. The vial was delivered to a 100 °C isotherm oven and heated for 24 h. Colorless cubic crystals were collected and washed with DMF

(3×5 mL). Yield: 70 mg (59% based on H_2PzDC). EA: Calcd for $C_{15}H_{25}N_7O_{13}Zn_3$: C, 25.46; H, 3.56; N, 13.86%. Found: C, 25.27; H, 4.56; N, 14.58%. FT-IR (KBr pellet) 3424 (br), 3129 (sh), 2956 (sh), 2803 (sh), 2487(sh), 1658 (sh), 1550 (vs), 1443 (s), 1342 (w), 1286 (s), 1051 (m), 1005 (m), 888 (w), 791 (s), 619 (w) cm^{-1}.

For porosity measurements, as-synthesized MOF-324 was rinsed with DMF and immersed in anhydrous methanol for 3 days, during which the activation solvent was decanted and freshly replenished three times. The solvent was removed under vacuum at 85 °C, yielding porous material.

$Cu_3[(Cu_3O)(PyC)_3(NO_3)]_2\cdot(DEF)_{18}(NMP)_3(H_2O)_8$, MOF-325. A solid mixture of $Cu(NO_3)_2\cdot2.5H_2O$ (170 mg, 0.73 mmol) and H_2PyC (30 mg, 0.27 mmol) were dissolved in DEF 7.5 mL and NMP 7.5 mL in a 20 mL vial. The vial was delivered to an 85 °C isotherm oven and heated for 24 h. Deep blue truncated octahedral crystals were collected and washed with DEF (3×5 mL). Yield: 81 mg (53% based on H_2PyC). EA: Calcd for $C_{129}H_{253}N_{35}O_{47}Cu_9$: C, 42.44; H, 6.99; N 13.43%. Found: C, 42.2; H, 7.15; N, 13.21%. FT-IR (KBr pellet) 3426 (br), 2976 (m), 2935 (m), 1662 (s), 1601 (m), 1540 (m), 1448 (m), 1387 (w), 1377 (w), 1296 (m), 1179 (w), 1118 (w), 1056 (w), 1005 (w), 888 (w), 817(w), 792 (m), 756 (w), 664 (w), 624 (w), 562 (w), 476 (w) cm^{-1}.

$Zn_4O(Et\text{-}PzDC)_3\cdot(DMF)_{16}(H_2O)_3$, MOF-326. A mixture of $Zn(NO_3)_2\cdot4H_2O$ (150 mg, 0.55 mmol) and $H_2Et\text{-}PzDC$ (50 mg, 0.14 mmol) were dissolved in DMF 15 mL in a 20 mL vial. The vial was delivered to a 100 °C isotherm oven and heated for 24 h. Colorless cubic crystals were collected and washed with DMF (3×5 mL). Yield: 51 mg (64% based on $H_2Et\text{-}PzDC$). EA: Calcd for $C_{96}H_{190}N_{28}O_{32}B_6Zn_4$: C, 44.78; H, 7.44; N, 15.23%. Found: C, 44.88; H, 7.16; N, 15.51%. FT-IR (KBr pellet) 3435 (br), 3134 (sh), 2946 (s), 2869 (sh), 1662 (s), 1561 (vs), 1454 (s), 1387 (w), 1306 (s), 1255 (s), 1107 (m), 1062 (w), 1016 (w), 909 (w), 853 (m), 787 (m), 664 (w) cm^{-1}.

For porosity measurements, as-synthesized MOF-326 was rinsed with DMF and immersed in chloroform for three days, during which the activation solvent was decanted and freshly replenished three times. The solvent was removed under vacuum at 85 °C, yielding porous material.

$Zn_4O(EDB)_3\cdot(DMF)_{17}(H_2O)_7$, IRMOF-61. *Single Crystal.* A mixture of H_2EDB (4.6 mg, 0.017 mmol) and $Zn(NO_3)_2\cdot4H_2O$ (17 mg, 0.064 mmol) was dissolved in DEF (1.0 mL) in a 4 mL vial. The vial was tightly capped with a Teflon-lined cap and placed in an 85 °C oven overnight. A crystal was mounted in a glass capillary, which was sealed with a small amount of mother liquor.

Bulk Scale. A mixture of H_2EDB (230 mg, 0.85 mmol) and $Zn(NO_3)_2\cdot4H_2O$ (810 mg, 3.1 mmol) was dissolved in DEF (75 mL) in a 120 mL vial fitted with a Teflon-lined cap. The solution was heated in an 85 °C oven for three days, after which time the hot mother liquor was decanted and DMF was added. PXRD analysis showed that the pattern matched the pattern simulated from single-crystal data. EA: Calcd for $C_{99}H_{157}N_{17}O_{37}Zn_4$: C, 48.75; H, 6.49; N, 9.76%. Found: C, 48.65; H, 6.46; N, 9.78%. FT-IR (KBr pellet) 2930 (m), 1663 (s), 1591 (s), 1546 (s) cm^{-1}.

For porosity measurements, as-synthesized IRMOF-61 was rinsed with DMF and immersed in dichloromethane. The solvent was exchanged three times over six days. The solvent was removed at 75 °C under vacuum, yielding the porous material.

Zn₄O(BDB)₃·(DMF)₁₀(H₂O)₃, IRMOF-62. *Single Crystal.* A mixture of H$_2$BDB (5.3 mg, 0.018 mmol) and Zn(NO$_3$)$_2$·4H$_2$O (15 mg, 0.057 mmol) was mixed in a pyrex tube with DEF (1.0 mL). The mixture was frozen (LN$_2$), evacuated to 15 mtorr, flame-sealed under static vacuum, thawed, and placed in an 85 °C oven for 6 days. A crystal was mounted in a glass capillary which was sealed with a small amount of mother liquor.

Solvothermal Synthesis. A mixture of H$_2$BDB (55 mg, 0.19 mmol), Zn(NO$_3$)$_2$·4H$_2$O (17 mg, 0.63 mmol), and triethylamine (22 μL) was mixed in DMF (20 mL) in a vial which was tightly capped. The mixture was sonicated for 15 min and placed in an 85 °C oven for 2 days, after which time the mother liquor was decanted and fresh DMF was added. PXRD analysis of the sample showed a match to the pattern simulated from the single-crystal data. EA: Calcd for C$_{84}$H$_{100}$N$_{10}$O$_{26}$Zn$_4$: C, 53.77; H, 5.28; N, 7.22%. Found: C, 52.49; H, 5.32; N, 7.26%. FT-IR (KBr) 2936 (m), 2223 (w), 2152 (w), 1678 (s), 1608 (s), 1550 (s) cm^{-1}.

For porosity measurements, as-synthesized IRMOF-62 was rinsed with DMF and immersed in dichloromethane. The solvent was exchanged three times over six days. The solvent was removed at 150 °C under vacuum, yielding the porous material.

Room Temperature Synthesis. A mixture of H$_2$BDB (10.2 g, 35.1 mmol) and Zn(OAc)$_2$·2H$_2$O was stirred in DMF (650 mL) for 16 h. A sample was collected for PXRD analysis. The peaks were found to match those of the simulated pattern. The powder was collected by filtration, rinsed with DMF and then with dichloromethane, and immersed in dichloromethane. The solvent was refreshed three times over six days. The product was filtered and activated under vacuum (15 mtorr) at 150 °C for 24 h, yielding the porous material.

■ RESULTS AND DISCUSSION

We focused on exploring the effects of specific attributes on hydrogen uptake, including nitrogen-containing, boron-containing, and alkyne-containing links, interpenetration, while also keeping in mind the goal of creating small pores resulting from choice of links and interpenetration. For our first strategy we chose pyrazabole-based links, containing both nitrogen and boron, in an effort to introduce greater polarizability. We found that in situ organic chemistry allowed us to generate and incorporate a smaller organic link, a pyrazole, into a framework, because solvothermal reactions sometimes cause unexpected organic reactions such as ligand oxidative coupling, hydrolysis, and substitution.[9] This allowed us to study the effects of enhanced polarizability and small pores.

The second strategy in our investigation involves using long alkyne-containing links instead of short ones, taking advantage of the potential for MOFs to form interpenetrated structures.[3b] The occurrence of catenation is strongly dependent on the connectivity of the building unit; for example, the **qom** net of MOF-177 is not allowed to form an interpenetrated structure,[3c,i] although the framework is comprised of large 1,3,5-benzenetribenzoate (BTB) links. In contrast, even short links, such as benzenedicarboxylate and acetylenedicarboxylate (Scheme 1), can form interpenetrated structures when the topology (connectivity) of the framework is highly symmetrical.[10,11] In our previous study, we have demonstrated that the total number of frameworks in a structure is influenced by not only the length of organic links but also the width of links and the diameter of the metal SBUs.[12] This means that highly interpenetrated MOFs will be formed if long, narrow links are

connected by symmetrical SBUs, such as Zn$_4$O(CO$_2$)$_6$ units. Therefore, we chose to use two organic links containing alkynes, ethynyldibenzoic acid, and butadiynedibenzoic acid (H$_2$EDB and H$_2$BDB), to increase the link lengths without increasing their widths, while simultaneously exploring the effects of alkyne units.

MOF-324. The SBU of MOF-324 is comprised of a trigonal pyramid Zn$_3$OH cluster, four PyC, and two HPyC groups to form only one kind of SBU (Figure 1), while no PzDC (pyrazabole dicarboxylate) is observed due to reaction of the organic starting material. In this SBU, three zinc atoms are bridged by three pyrazolates (i.e., deprotonated pyrazoles), while a μ_3-OH is placed above the triangle. Carboxylic moieties of two PyC and one HPyC are also coordinated to three Zn atoms. However, one carboxylic acid in the SBU is not deprotonated. The IR spectrum of solvent-free MOF-324 confirms the existence of a protonated carboxylic acid in the SBU (strong band at 1658 cm^{-1}). Since each SBU is connected to six neighboring SBUs through PyC linkers, MOF-324 has a primitive cubic (**pcu**) topology.[13] It should be noted that although MOF-324 has the same topology as MOF-5, the overall shorter linker achieved through use of two types of coordination to zinc leads to a much smaller pore diameter (7.6 Å for MOF-324, 9.5 Å for MOF-5[3a]).

As shown in Figure 1, although PzDC is used as a starting material, MOF-324 does not contain PzDC linkers. In general, although the transformation mechanism of organic compounds under solvothermal conditions is not clear,[14] it is hypothesized based on known chemistry that the Zn atom is inserted between B−N bonding by hydrolysis during the reaction and thereby forms the trinuclear Zn-complexes.[15] To appreciate the effectiveness of in situ ligand generation, H$_2$PyC and H$_2$Et-PzDC are employed under either the same or modified reaction conditions as control experiments. However, in all of our attempts, no crystals having small pores were obtained; MOF-324 is not produced using H$_2$PyC as a starting material with Zn. However, H$_2$PyC reacted with Cu(II) to form MOF-325, and MOF-326 was obtained from Zn and H$_2$Et-PzDC, which was found to be stable under the reaction conditions.

MOF-325. In contrast to MOF-324, MOF-325 was obtained using Cu(II) and H$_2$PyC as an organic linker (Figure 1).[16] This structure is constructed from two different SBUs; the carboxylates of metalloligands form a paddle wheel with Cu atoms possessing two solvent molecules at the axial positions of the paddle wheel unit, while three pyrazolate and Cu$_3$O pyramidal clusters form a triangular SBU (Figure 1) and solvent molecules are presumed to be coordinated to each Cu atom of a Cu$_3$O unit.[17] However, these solvents are highly disordered and could neither be identified nor located crystallographcally. If the paddle wheel units and Cu$_3$O pyramidal clusters can be considered to be planar square and triangular building units, respectively, a twisted boracite (**tbo**) three-dimensional structure is obtained. This connectivity is reminiscent of HKUST-1 comprised of Cu paddle wheel units and benzenetricarboxylates.[3d] Since the triangular metalloligand is even longer (11.1 Å) than benzene tricarboxylate (6.6 Å) in HKUST-1, the cavity of MOF-325 is larger than that in HKUST-1.

MOF-326. MOF-326 was synthesized from zinc and H$_2$Et-PzDC and was structurally characterized by X-ray diffraction. Unlike H$_2$PzDC, H$_2$Et-PzDC was not decomposed during the solvothermal reaction, and colorless cubic crystals were formed. MOF-326 has a neutral framework with Zn$_4$O units

octahedrally coordinated to Et-PzDC, which results in a **pcu** topology. Although MOF-326 has a long linker, it does not form interpenetrated frameworks. This is in sharp contrast to IRMOF-9, in which the length of the organic linker is nearly the same (distance between two carboxylate carbons for Et-PzDC and biphenyldicarboxylate are 9.62 and 10.1 Å, respectively).[3b] The four ethyl groups on the B atoms are directed into the pore, reducing the available space for interpenetration.

IRMOF-61. In IRMOF-61 $Zn_4O(CO_2)_6$ units are connected through EDB links.[18] The network topology is the same as that of IRMOF-1 (**pcu**). However, there are two differences compared to IRMOF-1. One is that two benzene rings in each EDB link along the *a*- and *b*-axes are twisted (90°), while the rings along the *c*-axis are coplanar. As a result, each single cubic framework has only one type of pore, unlike non-catenated IRMOFs.[3b] IRMOF-61 has a doubly interpenetrated structure to reduce free space; the length of the EDB link (distance between two carboxylate carbons for EDB is 12.6 Å) is even larger than biphenyldicarboxylate, which is already known to form a catenated framework (IRMOF-9).[3b] To our best knowledge, this is the first example by an IRMOF of catenation in between interpenetration and interweaving.[19]

Due to the twist of the EDB link, a weak, potential CH⋯π interaction between a benzene ring in the first framework and an H atom on a neighboring benzene ring in the second framework is observed (center-to-center distance between the benzene ring and an H atom is 3.79 Å). Consequently, the distance between the centers of alkynes at the cross is also small (3.68 Å). While neither of these interactions is strong enough to be full bonding interactions, we expect that the combination of interactions throughout the framework is significant enough to lead to the unusual interpenetration observed. Because of the interlocked framework in the *ab*-plane, the pore aperture along the *c*-axis is 6.1 Å. On the other hand, when the structure is viewed parallel to the (1 1 0) or (−1 1 0) directions, much larger rectangular channels are observed. The pores are thus ellipsoidal, with radii of 12.2 and 15.0 Å.

IRMOF-62. The longer BDB link allows for the resulting MOF to maintain the same cubic topology. However, in this structure, four cubes are packed in an unprecedented manner. The four cubic frameworks can be divided into two groups: set A (red and yellow frameworks in Figure 2B, C) and set B (green and blue frameworks). In each set, the two frameworks interweave in the same manner as IRMOF-9, 11, and 13;[3b] each edge is either parallel or perpendicular to edges in the second framework.[3b,12,20] Set A is rotated with respect to set B when we look at the yellow and blue frameworks. The two vertices of the second framework are almost on the two adjacent faces in the first cubic framework. The remaining four vertices of the second framework penetrate four of six faces in the first framework. Therefore, the faces of each cubic framework contain two vertices and four edges of the second framework (and vice versa). The relationship between sets A and B is much more complicated compared to the usual interpenetration topology of the **pcu** nets.[21,22] The four frameworks are inseparable without breaking bonds since each framework grows through all three of the others. For instance, four of the six faces in the red cubic framework have one vertex from set B frameworks (blue) and two penetrating edges (yellow and green), and the remaining two faces have three penetrating edges (yellow, blue, and green). The reason why IRMOF-62 shows a unique interpenetration mode is not clear, but it seems
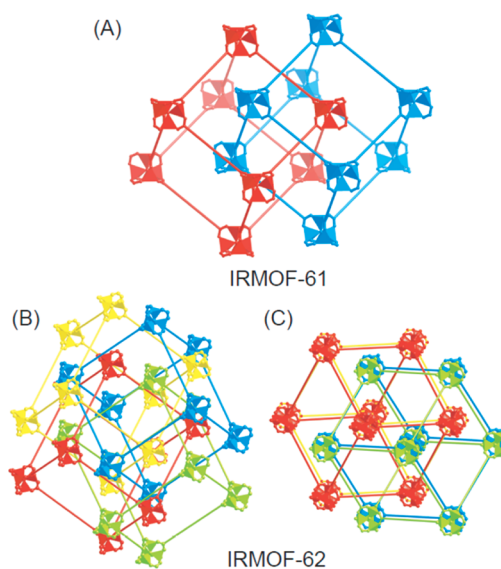

Figure 2. Schematic drawings of the framework interpenetration in IRMOF-61 (A) and IRMOF-62 (B, C). Lines represent the alkyne links. (B, C) Set A, red/yellow, and set B, green/blue, are rotated with respect to each other.

that each BDB link forms a CH⋯π interaction between sets A and B, whose distance of 2.96 Å is even shorter than that of IRMOF-61.

Due to the complicated interpenetration, it is difficult to estimate their pore aperture and diameter. The micropore seems to be connected discontinuously; however, a characteristic 1D channel along the crystallographic *c*-axis is observed. In Table 2, we used the 1D channel for the estimation of the pore diameter and aperture (5.2 Å).

Table 2. Summary of Surface Areas (A), Pore Diameters (d_p), and Pore Apertures (d_a) for Materials in This Study[a,b]

MOF	d_p/Å	d_a/Å	A_{Lang}/ $m^2 \, g^{-1}$	A_{BET}/ $m^2 \, g^{-1}$	V_p/ $cm^3 \, g^{-1}$	d_{bulk}/ $g \, cm^{-3}$
MOF-324	7.6	5.8	1780	1600	0.59	0.884
MOF-325	19.6	8.2	<10	<10	n.d.	0.477
MOF-326	15.4	7.8	1680	1380	0.55	0.481
IRMOF-61	12.2, 15.0	10.6	1580	1410	1.66	0.464
IRMOF-62	5.2	5.2	2690	2420	0.91	0.691

[a]Acronyms: A_{Lang} and A_{BET} are the Langmuir and BET surface areas; V_p is the measured total pore volume; d_{bulk} is the crystal density of the evacuated materials. [b]Pore diameter, aperture, and density were calculated from their crystal structures. The pore diameters are measured in Cerius[2] as the largest sphere that does not contact the van der Waals radii of any of the framework atoms.

Porosity and Architectural Stability. Thermal gravimetric analysis (TGA) was used to evaluate the framework stability under solvent-exchange conditions. Indeed, MOF-324 and 326 do not show any weight loss up to 250 °C except for the loss of occluded activation solvents below 100 °C. Activated IRMOF-61 and 62 show no weight loss up to 350 °C.[23]

To determine whether the MOFs can maintain their structural integrity in the absence of guests and whether the small pores inhibit the diffusion of guest molecules, we examined the gas sorption behavior of these compounds. Ar

sorption in MOF-324 shows a reversible Type I isotherm at 87 K, which indicates that this compound possesses permanent porosity (Figure 3). The apparent surface area and pore volume
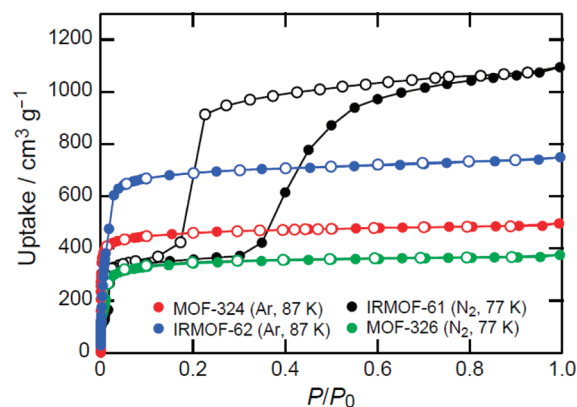

Figure 3. Ar adsorption isotherms of MOF-324 (red) and IRMOF-62 (blue) at 87 K and N_2 isotherms of MOF-326 (green) and IRMOF-61 (black) at 77 K. Filled and open circles represent adsorption and desorption branches. Connecting lines are guides for the eye.

based on the Dubinin−Radushkevich (DR) plot method for MOF-324 were estimated to be 1780 m^2 g^{-1} and 0.59 cm^3 g^{-1}, respectively, from these data. In the case of MOF-326, a steep N_2 uptake was observed in the low-pressure region accompanied by a small step at P/P_0 = 0.01. The small hysteresis ranging from P/P_0 = 0.1 to 0.3 may be attributed to the flexibility of the framework due to the long organic linker with protruding ethyl groups. The Langmuir surface area of MOF-326 calculated from the N_2 uptake is 1680 cm^2 g^{-1}, and the estimated pore volume was found to be 0.55 cm^3 g^{-1}. MOF-325 did not show permanent porosity (<10 m^2 g^{-1}) in our experiments despite the fact that the crystal structure implies that there is enough void space for gas diffusion. It is presumed that the triangular cluster of MOF-325 may not be sufficiently rigid to support permanent porosity.

The profile of the N_2 (77 K) isotherm for IRMOF-61 is unique for IRMOFs; there is a small step at P/P_0 = 0.015 followed by a large step (P/P_0 = 0.4) with an unusual hysteresis (Figure 3). N_2 uptake at the first step (150 cm^3 g^{-1}) corresponds to 7 N_2 molecules in each formula unit $(Zn_4O(EDB)_3)$. If the a- and b-sites on a Zn_4O unit are occupied,[24] N_2 density around the interweaving section (i.e., a small pore along the c-axis) can be higher than other adsorption sites, and this could be the driving force[25] of a guest-induced structural transition[26] and/or framework shifting during uptake (e.g., a gating phenomenon).[27] In contrast, N_2 uptake below the second step (350 cm^3 g^{-1}) corresponds to 16 N_2 molecules in each formula unit. Although there is no information about

specific adsorption sites for N_2, it is likely that the most of the strong binding sites in IRMOF-61 should be occupied by N_2 molecules. Therefore, we attribute the second hysteresis to a phase transition of guest molecules in the pore,[28] a known but uncommon phenomenon in MOFs. The total N_2 uptake reached was 1070 cm^3 g^{-1} at P/P_0 = 0.95 due to the small bulk density (0.464 g cm^{-3}), which is comparable to the highly porous material of MOF-177 (1250 cm^3 g^{-1} for N_2 uptake, 0.426 g cm^{-3} for density), despite the interpenetration.[3c,6b]

Ar adsorption of IRMOF-62 followed a reversible isotherm at 87 K with a small step in the range from P/P_0 = 0.01 to 0.03. The adsorbed amounts of Ar below the step (ca. 330 cm^3 g^{-1}) correspond to 17 Ar molecules in each formula unit $(Zn_4O(BDB)_3)$. Considering that the N_2 isotherm for IRMOF-62 also shows a similar second step when almost the same amount of N_2 is adsorbed,[23] it is presumed that there are binding sites for Ar and N_2 in the framework. The second step should be attributed to the micropore filling rather than to strong interaction between IRMOF-62 and Ar. Indeed, the pore size distribution based on the Ar isotherm is much larger than the pore diameter estimated from the crystal structure. This may indicate that interactions between the alkyne (i.e., edge) and Ar are not strong; therefore, greater pressure could be necessary to complete the micropore filling.

From the N_2 or Ar adsorption isotherms, the apparent surface areas (Langmuir model) and total pore volumes of each material have been estimated (Table 2). The pore volume of each material was estimated by a DR model with the assumption that the adsorbate is in the liquid state and the sorption involves a pore-filling process. The BET surface areas (accessible surface area) for MOFs are also presented in Table 2.

Low-Pressure H_2 Isotherms and Adsorption Enthalpies. Based on the crystal structures and N_2/Ar isotherms for four MOFs, it can be said that activated MOF-324 and IRMOF-62 samples have smaller pore diameters while maintaining surface areas. To investigate the usefulness of smaller pore materials, low-pressure H_2 isotherms were obtained.

Table 3 summarizes hydrogen uptake for these new MOFs, with MOF-177 data shown for comparison. In addition, Figure 4A shows H_2 adsorption isotherms for four MOFs (at 77 K) which are constructed by octahedrally linked $Zn_4O(CO_2)_6$ clusters with organic units. Under these conditions, H_2 adsorption isotherms are not fully saturated, because the temperature is well above the critical temperature.[4,29] There is no specific relationship between H_2 uptakes and surface areas. MOF-324 outperforms the other new MOFs in the pressure range from 100 to 800 torr, and the H_2 uptake at 760 torr decreases from IRMOF-62 to IRMOF-61 to MOF-326. The uptake of H_2 for MOF-324 at 760 torr was found to be 21 mg

Table 3. H_2 Adsorption for MOFs in This Study[a,6b]

MOF	H_2 uptake at 760 torr and 77 K/mg g^{-1}	Q_{st}/kJ mol^{-1b}	surface excess H_2 uptake (pressure)			total H_2 uptake (pressure)		
			mg g^{-1}	g L^{-1}	bar	mg g^{-1}	g L^{-1}	bar
MOF-177	12.5	4.4	75	32	(69)	114	49	(78)
MOF-324	21.0	6.2	33	30	(33)	47	42	(79)
MOF-326	9.2	7.1	n.d.			n.d.		
IRMOF-61	10.7	7.4	n.d.			n.d.		
IRMOF-62	17.2	7.3	48	33	(39)	68	47	(76)

[a]MOF-177 data is presented for comparison. [b]Q_{st} values calculated at near-zero H_2 coverage.

13148

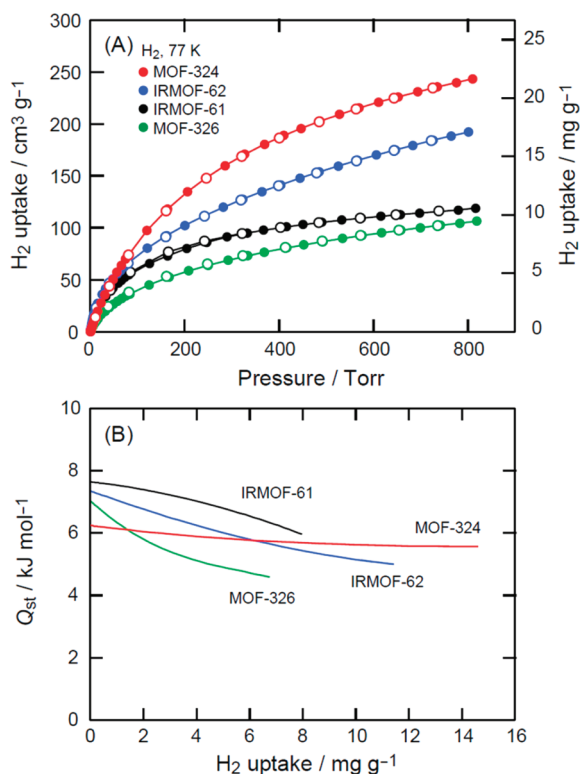dx.doi.org/10.1021/jp302356q | J. Phys. Chem. C 2012, 116, 13143−13151

Figure 4. (a) Low-pressure H_2 isotherms of MOFs at 77 K. All symbols are the same as in Figure 3. Connecting lines are guides for the eye. (b) Coverage dependencies of the isosteric heat of adsorption for H_2 in MOFs calculated from fits of its 77 and 87 K isotherms.

g^{-1}. This is slightly lower than that in MOF-505 and HKUST-1 (24 and 25 mg g^{-1}), materials with open metal sites, but much higher than that in MOF-5 and MOF-177 (13 and 12 mg g^{-1}) in this low-pressure region.[4,6a,29]

To further investigate the interaction between adsorbent and H_2 molecules, H_2 adsorption isotherms were collected at 77 and 87 K for IRMOF-61, IRMOF-62, MOF-324, and MOF-326.[23,30] Figure 4B demonstrates the coverage dependencies of Q_{st} calculated from fitting the 77 and 87 K data. IRMOF-61, IRMOF-62, and MOF-326 show near-zero coverage Q_{st} values of 7.4, 7.3, and 7.1 kJ mol^{-1}, respectively, which are greater than those of MOF-177, MOF-5, and HKUST-1 (4.4, 4.9, and 6.9 kJ mol^{-1}) but less than those of MOF-74 and IRMOF-11 (7.9, and 9.1 kJ mol^{-1}).[6a,b] In the case of MOF-324, the initial Q_{st} (6.2 kJ mol^{-1}) is lower than those of IRMOF-62 and MOF-326. This suggests that pore environments near the Zn_4O units are more suitable toward H_2 binding than the Zn_3OH unit in MOF-324 at low coverage. However, it is worth noting that the Q_{st} for MOF-324 is not substantially influenced by the surface coverage of H_2 (5.6 kJ mol^{-1} at 15 mg g^{-1} of surface coverage). We attribute this effect to the small pore diameter in MOF-324, which facilitates stronger binding of H_2 by interactions with many more surface sites. This is in sharp contrast to MOF-326, in which the boron and nitrogen atoms in the link are negatively and positively charged, respectively; MOF-326 shows a gradual decrement to 4.5 kJ mol^{-1} at 7 mg g^{-1} of surface coverage, as the polarized B−N bonds appear to improve the H_2 binding energy with respect to simple aromatic units seen in previous MOFs. In IRMOF-62, with its complicated pore structure, H_2 is expected to be adsorbed on the stronger binding sites (e.g., Zn_4O unit[31,32]) first, followed

by less strong binding in the more open pores of the MOF, which is consistent with the moderate decrement of the Q_{st}. A similar initial binding energy is seen for IRMOF-61. We attribute the near-zero coverage values to stronger binding at the Zn clusters facilitated by the closeness of clusters due to interpenetration in each material. At higher coverage, the binding energy decreases to approximately 5 kJ mol^{-1} for IRMOF-62 and approximately 6 kJ mol^{-1} for IRMOF-61. In both cases, the binding energies are still greater than that of MOF-177 at higher coverage, which we hypothesize can be attributed to the alkynes; because IRMOF-61 has much larger pores than IRMOF-62, the best explanation for their respective binding energies so far is the fact that they both contain carbon−carbon triple bond units.

High-Pressure H_2 Storage. MOF-324 and IRMOF-62 were investigated for their high-pressure H_2 capacities at 77 and 298 K (Figure 5A). The gravimetric excess H_2 uptakes at 77 K
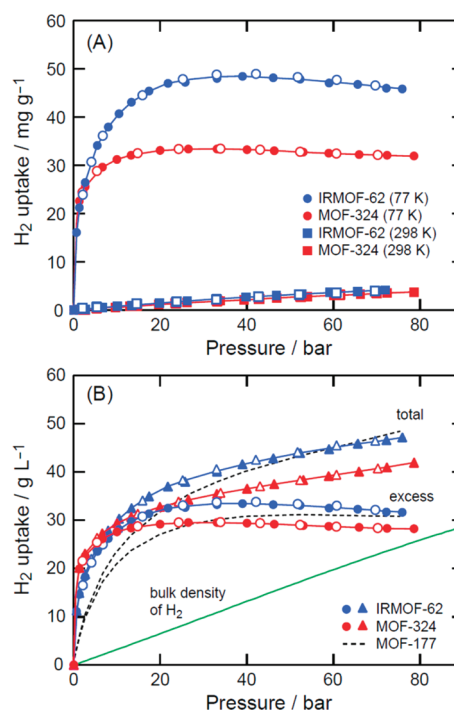

Figure 5. (a) High-pressure H_2 excess uptakes for MOF-324 (red) and IRMOF-62 (blue) in gravimetric unit collected at 77 (circles) and 298 K (squares). (b) Surface excess (circles) and total (triangles) H_2 uptake in MOF-324 (red) and IRMOF-62 (blue) at 77 K are converted in the volumetric unit. Data for MOF-177 (black broken curves)[6b] and the bulk density of H_2 at the same temperature (green curve) are shown for comparison. Filled and open circles represent adsorption and desorption branches. Connecting lines are guides for the eyes.

for MOF-324 and IRMOF-62 are 33 and 49 mg g^{-1}, respectively. These are only modest gravimetric uptakes compared to 75 mg g^{-1} for MOF-177 at approximately 70 bar, because excess H_2 uptake in the high-pressure region is substantially dependent on the surface area (or micropore volume) of MOF rather than adsorption enthalpy.[33,34] Although the surface excess mass is a useful concept, from the viewpoint of H_2 storage, the total amount that a material can store is more relevant to use for H_2 as a fuel. Since the total adsorbed amount cannot be measured experimentally, we estimate the total uptake of H_2 using a pore volume of MOFs

and bulk H_2 density ($N_{total} = N_{ex} + \rho_{bulk}V_{p,DR}$).[6b,c] Figure 5B demonstrates the total uptake of H_2 in volumetric units (g L^{-1}). By this metric, the MOF materials are much more similar in their hydrogen uptake capacities.[34] Indeed, the total H_2 uptake in IRMOF-62 (volumetric units) is even greater than that in MOF-177 up to 60 bar. This clearly demonstrates that highly interpenetrating structures do not always have a negative impact on the gas storage capacity, but that interpenetration is a highly useful attribute for obtaining high hydrogen capacity.

As shown in Figure 5, MOF-324 and IRMOF-62 show lower saturation pressures (39 bar) than that for MOF-177, as predicted from their greater binding energies for H_2. To illustrate their reversible and fast hydrogen uptake (and release), a time course profile of adsorption and successive desorption processes in IRMOF-62 was recorded,[23] showing that adsorption and desorption processes are almost complete within 5 min even though a large pressure change (2−53 bar) is applied to the experimental system. This clearly demonstrates that the interpenetration does not disturb fast gas diffusion in micropores.

Inelastic Neutron-Scattering Study of the Rotational Transition of Hydrogen Adsorbed in MOF-324. Further details about the binding of H_2 in MOF-324 were derived from inelastic neutron-scattering (INS) experiments.[31] The INS spectrum of one, two, and three hydrogen molecules per formula unit adsorbed in MOF-324 is shown in Figure 6. The
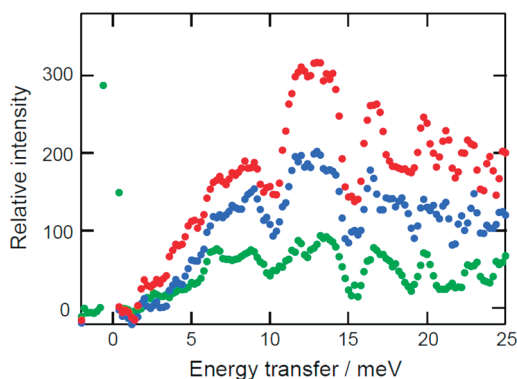

Figure 6. INS spectra for one (green), two (blue), and three (red) hydrogen molecules per formula unit adsorbed in MOF-324.

two most noteworthy aspects of these spectra when compared to those obtained for MOF-5, for example, are the broadening of the peaks and the significant amount of intensity found at energies less than 10 meV. The width of the bands suggests that the binding sites are not as well-defined as in MOF-5, most likely because the smaller channels subject the hydrogen molecules to additional interactions, so that it can take up a variety of favorable binding sites. The occurrence of transitions at lower energy implies the presence of sites with stronger interactions between hydrogen and host material, which we may also attribute to the smaller pore sizes. We can identify at least four different H_2 binding sites at the lowest loading, and note that the intensities of all the peaks associated with these sites (i.e., their population) increase at similar rates with increases in H_2 loading to two molecules per formula unit. This observation is in accord with the rather weak dependence of Q_{st} on H_2 coverage described above.

In analogy with the primary binding site in MOF-5, we attribute the peak at the lowest energy, i.e., 6.4 meV, to

hydrogen molecules adsorbed at a site on the metal cluster. The rotational transition frequency for the pocket site on the cluster in MOF-5 is 10.3 meV, which corresponds to a twofold barrier to rotation of 1.8 kJ mol^{-1} vs 3.7 kJ mol^{-1} in MOF-324. The much stronger interaction in MOF-324 is reflected in the low-coverage heat of adsorption of 6.2 kJ mol^{-1} compared with 4.8 kJ mol^{-1} in MOF-5. Two other sites with strong interactions of H_2 are found to be occupied at low loadings, whereas at higher loadings the transition energies observed (11−14 meV) reflect those identified by us for sites near and on the organic linkers.

CONCLUSIONS

We have explored the use of new functionalities and resulting pore-size control toward improving hydrogen uptake. With MOF-324, we demonstrate the usefulness of generating a short link in situ to form a MOF with a small pore diameter, which exhibits excellent cryogenic H_2 (77 K) uptake at 760 torr. The hydrogen uptake in MOF-326 indicates that more polarizable links are indeed beneficial toward hydrogen uptake through improved interactions with the guests at higher loading. IRMOF-61 and 62 show evidence that long links can be used to generate highly interpenetrated structures with novel modes of interpenetration, allowing for control of pore dimensions and density of adsorptive sites that prove advantageous as part of the greater scheme for improving hydrogen uptake in MOFs. More importantly, IRMOF-62 shows volumetric H_2 uptake capacity on par with MOF-177 at high pressures, including improved energy of interaction and higher uptake than MOF-177 up to 60 bar, due to the ideal pore diameters for H_2 storage. The small pore of IRMOF-62 (5.2 Å) has no negative impact on fast gas diffusion.

ASSOCIATED CONTENT

S Supporting Information

Details of the single-crystal X-ray data collection and analysis for five MOFs, powder X-ray diffraction patterns (simulated and experimental), TGA traces, N_2/Ar (semilogarithmic scale) and low-pressure H_2 isotherms at 77 and 87 K for MOF-324, 326 and IRMOF-61, 62, the time course profile of H_2 uptake for IRMOF-62, synthetic procedures and characterization of H_2EDB and H_2BDB, and complete ref 3i. This material is available free of charge via the Internet at http://pubs.acs.org.

AUTHOR INFORMATION

Corresponding Author

*E-mail: furukawa@chem.ucla.edu.

Present Address

[⊥]Department of Chemistry, University of California and The Molecular Foundry at Lawrence Berkeley National Laboratory, Berkeley, CA 94720, United States.

Notes

The authors declare no competing financial interest.

ACKNOWLEDGMENTS

benefited from the use of facilities at the Intense Pulsed Neutron Source, a national user facility funded as such by the Office of Science, U.S. DOE.

■ REFERENCES

(1) (a) Satyapal, S.; Petrovic, J.; Read, C.; Thomas, G.; Ordaz, G. *Catal. Today* **2007**, *120*, 246−256. (b) IPCC 2007; *Climate Change 2007: Synthesis Report*; Pachauri, R. K., Reisinger, A., Eds.; IPCC: Geneva, Switzerland, 2008.

(2) (a) Suh, M. P.; Park, H. J.; Prasad, T. K.; Lim, D.-W. *Chem. Rev.* **2012**, *112*, 782−835. (b) Ma, S.; Zhou, H.-C. *Chem. Commun.* **2010**, *46*, 44−53. (c) Murray, L. J.; Dincă, M.; Long, J. R. *Chem. Soc. Rev.* **2009**, *38*, 1294−1314.

(3) (a) Li, H.; Eddaoudi, M.; O'Keeffe, M.; Yaghi, O. M. *Nature* **1999**, *402*, 276−279. (b) Eddaoudi, M.; Kim, J.; Rosi, N.; Vodak, D.; Wachter, J.; O'Keeffe, M.; Yaghi, O. M. *Science* **2002**, *295*, 469−472. (c) Chae, H. K.; Siberio-Pérez, D. Y.; Kim, J.; Go, Y.; Eddaoudi, M.; Matzger, A. J.; O'Keeffe, M.; Yaghi, O. M. *Nature* **2004**, *427*, 523−527. (d) Chui, S. S.-Y.; Lo, S. M.-F.; Charmant, J. P. H.; Orpen, A. G.; Williams, I. D. *Science* **1999**, *283*, 1148−1150. (e) Yan, Y.; Lin, X.; Yang, S.; Blake, A. J.; Dailly, A.; Champness, N. R.; Hubberstey, P.; Schröder, M. *Chem. Commun.* **2009**, 1025−1027. (f) Dincă, M.; Long, J. R. *Angew. Chem., Int. Ed.* **2008**, *47*, 6766−6779. (g) Sun, D.; Ma, S.; Ke, Y.; Collins, D. J.; Zhou, H.-C. *J. Am. Chem. Soc.* **2006**, *128*, 3896−3897. (h) Férey, G.; Mellot-Draznieks, C.; Serre, C.; Millange, F.; Dutour, J.; Surblé, S.; Margiolaki, I. *Science* **2005**, *309*, 2040−2042. (i) Furukawa, H.; et al. *Science* **2010**, *329*, 424−428. (j) Klein, N.; Senkovska, I.; Gedrich, K.; Stoeck, U.; Henschel, A.; Mueller, U.; Kaskel, S. *Angew. Chem., Int. Ed.* **2009**, *48*, 9954−9957.

(4) Chen, B.; Ockwig, N. W.; Millward, A. R.; Contreras, D. S.; Yaghi, O. M. *Angew. Chem., Int. Ed.* **2005**, *44*, 4745−4749.

(5) (a) Lowell, S.; Shields, J. E.; Thomas, M. A.; Thommes, M. *Characterization of Porous Solids and Powders: Surface Area, Pore Size and Density*, Kluwer Academic Publishers: Dordrecht, The Netherlands, 2004. (b) Rouquerol, F.; Rouquerol, J.; Sing, K. *Adsorption by Powders & Porous Solids*; Academic Press: London, U.K., 1999.

(6) (a) Rowsell, J. L. C.; Yaghi, O. M. *J. Am. Chem. Soc.* **2006**, *128*, 1304−1315. (b) Furukawa, H.; Miller, M. A.; Yaghi, O. M. *J. Mater. Chem.* **2007**, *17*, 3197−3204. (c) Furukawa, H.; Yaghi, O. M. *J. Am. Chem. Soc.* **2009**, *131*, 8875−8883.

(7) (a) Trofimenko, S. *J. Am. Chem. Soc.* **1967**, *89*, 4948−4952. (b) Trofimenko, S. *J. Am. Chem. Soc.* **1967**, *89*, 3165−3170. (c) Trofimenko, S. *J. Org. Chem.* **1963**, *28*, 2755−2758.

(8) Kraus, W.; Nolze, G. *J. Appl. Crystallogr.* **1996**, *29*, 301−303.

(9) (a) Goodgame, D. M. L.; Grachvogel, D. A.; Williams, D. J. *Angew. Chem., Int. Ed.* **1999**, *38*, 153−156. (b) Tao, J.; Zhang, Y.; Tong, M.-L.; Chen, X.-M.; Yuen, T.; Lin, C. L.; Huang, X.; Li, J. *Chem. Commun.* **2002**, 1342−1343. (c) Xiong, R.-G.; Zhang, J.; Chen, Z.-F.; You, X.-Z.; Che, C.-M.; Fun, H.-K. *J. Chem. Soc., Dalton Trans.* **2001**, 780−782. (d) Feller, R. K.; Forster, P. M.; Wudl, F.; Cheetham, A. K. *Inorg. Chem.* **2007**, *46*, 8717−8721. (e) Zhao, D.; Yuan, D.; Yakovenko, A.; Zhou, H.-C. *Chem. Commun.* **2010**, *46*, 4196−4198.

(10) Hafizovic, J.; Bjørgen, M.; Olsbye, U.; Dietzel, P. D. C.; Bordiga, S.; Prestipino, C.; Lamberti, C.; Lillerud, K. P. *J. Am. Chem. Soc.* **2007**, *129*, 3612−3620.

(11) Tranchemontagne, D. J.; Hunt, J. R.; Yaghi, O. M. *Tetrahedron* **2008**, *64*, 8553−8557.

(12) Reineke, T. M.; Eddaoudi, M.; Moler, D.; O'Keeffe, M.; Yaghi, O. M. *J. Am. Chem. Soc.* **2000**, *122*, 4843−4844.

(13) The three letter designators generally given for important common nets as outlined in Reticular Chemistry Structure Resource (RCSR); http://rcsr.anu.edu.au/: O'Keeffe, M.; Peskov, M. A.; Ramsen, S. J.; Yaghi, O. M. *Acc. Chem. Res.* **2008**, *41*, 1782−1789.

(14) Katritzky, A. R.; Nichols, D. A.; Siskin, M.; Murugan, R.; Balasubramanian, M. *Chem. Rev.* **2001**, *101*, 837−892.

(15) Norwood, V. M., III; Morse, K. W. *Inorg. Chem.* **1987**, *26*, 284−288.

(16) Procopio, E. Q.; Linares, F.; Montoro, C.; Colombo, V.; Maspero, A.; Barea, E.; Navarro, J. A. R. *Angew. Chem., Int. Ed.* **2010**, *49*, 7308−7311.

(17) (a) Mezei, G.; McGrady, J. E.; Raptis, R. G. *Inorg. Chem.* **2005**, *44*, 7271−7273. (b) Mezei, G.; Rivera-Carrillo, M.; Raptis, R. G. *Dalton Trans.* **2007**, 37−40.

(18) (a) Pham, B. T. N.; Lund, L. M.; Song, D. *Inorg. Chem.* **2008**, *47*, 6329−6335. (b) Gadzikwa, T.; Zeng, B.-S.; Hupp, J. T.; Nguyen, S. T. *Chem. Commun.* **2008**, 3672−3674.

(19) Rowsell, J. L. C.; Yaghi, O. M. *Angew. Chem., Int. Ed.* **2005**, *44*, 4670−4679.

(20) Kesanli, B.; Cui, Y.; Smith, M. R.; Bittner, E. W.; Bockrath, B. C.; Lin, W. *Angew. Chem., Int. Ed.* **2005**, *44*, 72−75.

(21) Batten, S. R. *CrystEngComm* **2001**, *18*, 1−7.

(22) Hong, C. S.; Son, S.-K.; Lee, Y. S.; Jun, M.-J.; Do, Y. *Inorg. Chem.* **1999**, *38*, 5602−5610.

(23) See Supporting Information for details.

(24) Rowsell, J. L. C.; Spencer, E. C.; Eckert, J.; Howard, J. A. K.; Yaghi, O. M. *Science* **2005**, *309*, 1350−1354.

(25) We do not know how the structural transition of IRMOF-61 occurs; however, it should be noted that a small, but unusual, hysteresis loop was also observed for low-pressure H_2 isotherms at 77 and 87 K (Figure S37). Since H_2 is not condensed in the pore under the present experimental conditions, no phase transition of H_2 in the pore should be observed. Therefore, the hysteresis loop of the H_2 isotherms should be attributed to the framework−guest interaction, where part of the heat of H_2 adsorption was used for the structural transition. The heat of H_2 adsorption is generally smaller than that of N_2 so that it should be easy to gain enough energy to cause the structural transition by the adsorption of N_2.

(26) (a) Kitaura, R.; Fujimoto, K.; Noro, S.; Kondo, M.; Kitagawa, S. *Angew. Chem., Int. Ed.* **2002**, *41*, 133−135. (b) Cussen, E. J.; Claridge, J. B.; Rosseinsky, M. J.; Kepert, C. J. *J. Am. Chem. Soc.* **2002**, *124*, 9574−9581. (c) Tanaka, D.; Nakagawa, K.; Higuchi, M.; Horike, S.; Kubota, Y.; Kobayashi, T. C.; Takata, M.; Kitagawa, S. *Angew. Chem., Int. Ed.* **2008**, *47*, 3914−3918. (d) Coudert, F.-X.; Jeffroy, M.; Fuchs, A. H.; Boutin, A.; Mellot-Draznieks, C. *J. Am. Chem. Soc.* **2008**, *130*, 14294−14302.

(27) (a) Kitaura, R.; Seki, K.; Akiyama, G.; Kitagawa, S. *Angew. Chem., Int. Ed.* **2003**, *42*, 428−431. (b) Kondo, A.; Noguchi, H.; Carlucci, L.; Proserpio, D. M.; Ciani, G.; Kajiro, H.; Ohba, T.; Kanoh, H.; Kaneko, K. *J. Am. Chem. Soc.* **2007**, *129*, 12362−12363. (c) Chen, B.; Liang, C.; Yang, J.; Contreras, D. S.; Clancy, Y. L.; Lobkovsky, E. B.; Yaghi, O. M.; Dai, S. *Angew. Chem., Int. Ed.* **2006**, *45*, 1390−1393.

(28) (a) Lincke, J.; Lässig, D.; Moellmer, J.; Reichenbach, C.; Puls, A.; Moeller, A.; Gläser, R.; Kalies, G.; Staudt, R.; Krautscheid, H. *Microporous Mesoporous Mater.* **2011**, *142*, 62−69. (b) Reichenbach, C.; Kalies, G.; Lincke, J.; Lässig, D.; Krautscheid, H.; Moellmer, J.; Thommes, M. *Microporous Mesoporous Mater.* **2011**, *142*, 592−600.

(29) Rowsell, J. L. C.; Millward, A. R.; Park, K. S.; Yaghi, O. M. *J. Am. Chem. Soc.* **2004**, *126*, 5666−5667.

(30) (a) Czepirski, L.; Jagiello, J. *Chem. Eng. Sci.* **1989**, *44*, 797−801. (b) Jagiello, J.; Bandosz, T. J.; Putyera, K.; Schwarz, J. A. *J. Chem. Eng. Data* **1995**, *40*, 1288−1292.

(31) (a) Rowsell, J. L. C.; Eckert, J.; Yaghi, O. M. *J. Am. Chem. Soc.* **2005**, *127*, 14904−14910. (b) Rosi, N. L.; Eckert, J.; Eddaoudi, M.; Vodak, D. T.; Kim, J.; O'Keeffe, M.; Yaghi, O. M. *Science* **2003**, *300*, 1127−1129.

(32) Spencer, E. C.; Howard, J. A. K.; McIntyre, G. J.; Rowsell, J. L. C.; Yaghi, O. M. *Chem. Commun.* **2006**, 278−280.

(33) Wong-Foy, A. G.; Matzger, A. J.; Yaghi, O. M. *J. Am. Chem. Soc.* **2006**, *128*, 3494−3495.

(34) Frost, H.; Düren, T.; Snurr, R. Q. *J. Phys. Chem. B* **2006**, *110*, 9565−9570.

13151

dx.doi.org/10.1021/jp302356q | *J. Phys. Chem. C* 2012, 116, 13143−13151